Full-beam performances of a PET detector with synchrotron therapeutic proton beams

M. A. Piliero[1], F. Pennazio[3], M. G. Bisogni[1], N. Camarlinghi[1], P.G. Cerello[2,3], A. Del Guerra[1], V. Ferrero[2,3], E. Fiorina[3], G. Giraudo[3], M. Morrocchi[1], C. Peroni[2,3], G. Pirrone[1], G. Sportelli[1], R. Wheadon[3]

[1]Department of Physics, University of Pisa, Pisa, Italy and INFN, Pisa, Italy
[2]Department of Physics, University of Torino, Torino, Italy
[3]INFN, Torino, Italy

Abstract

Treatment quality assessment is a crucial feature for both present and next-generation ion therapy facilities. Several approaches are being explored, based on prompt radiation emission or on PET signals by β^+-decaying isotopes generated by beam interactions with the body.

In-beam PET monitoring at synchrotron-based ion therapy facilities has already been performed, either based on inter-spill data only, to avoid the influence of the prompt radiation, or including both in-spill and inter-spill data. However, the PET images either suffer of poor statistics (inter-spill) or are more influenced by the background induced by prompt radiation (in-spill). Both those problems are expected to worsen for accelerators with improved duty cycle where the inter-spill interval is reduced to shorten the treatment time. With the aim of assessing the detector performance and developing techniques for background reduction, a test of an in-beam PET detector prototype was performed at the CNAO synchrotron-based ion therapy facility in full-beam acquisition modality.

Data taken with proton beams impinging on PMMA phantoms showed the system acquisition capability and the resulting activity distribution, separately reconstructed for the in-spill and the inter-spill data. The Coincidence Time Resolution for in-spill and inter-spill data shows a good agreement, with a slight deterioration during the spill. The data selection technique allows the identification and rejection of most of the background originated during the beam delivery. The activity range difference between two different proton beam energies (68 and 72 MeV) was measured and found to be in sub-millimeter agreement with the expected result.

However, a slightly longer (2 mm) absolute profile length is obtained for in-spill data when compared to inter-spill data.

1 Introduction

The main advantage of treating a cancer with proton or ion beams rather than conventional photon beams is the ability to deliver a high radiation dose to the tumour volume while sparing the healthy tissues. The energy deposition of charged particles in matter, described by the Bragg curve, is characterized by a pronounced peak at the end of the particle range. In a clinical setting this feature allows the delivery of a high radiation dose to the tumour volume with a low entrance and exit dose. Therefore proton and ion beam treatments are characterized by sharp dose gradients: for this reason current clinical practice makes use of large safety margins (3.5 % + 3 mm) around the tumour. In fact the sharpness of the Bragg peak is seldom utilized to prevent high dose to critical structures close to the tumour in case of beam over-ranges (Parodi 2016). To fully exploit the advantage of ion therapy an *in-vivo* monitoring of the particle range in tissue would be highly desirable. Since the primary beam is completely stopped inside the patient, the only way to non-invasively verify the particle range is to collect the secondary radiation generated by the beam-tissue interactions that exits the patient body.

Among the solutions proposed for the *in-vivo* particle range verification (Enghardt et al. 2004), a promising one is based on the detection of high energy photons emitted promptly by the target nuclei which are left in an excited state after the interactions with the beam. The development of detector systems for prompt gamma imaging (PGI) (Kim et al. 2009, Lee et al. 2013, Perali et al. 2014, McCleskey et al. 2015, Llosá et al. 2013, Roellinghoff et al. 2011, Kormoll et al. 2011), timing (Golnik et al. 2014) and spectroscopy (Verburg and Seco 2014) is rapidly growing but only recently a PGI system prototype based on a knife-edge slit camera has been used in a clinical pilot study at the Universitäts Protonen Therapie Dresden (UDTP) (Richter et al. 2016).

In practice the only *in-vivo* non invasive monitoring technique largely investigated in clinic is based on the well established diagnostic imaging technique Positron Emission Tomography (PET) (Del Guerra et al. 2016) . In this case the role of the radiotracer is taken by the β^+ emitters produced by nuclear fragmentation reactions between the therapeutic beam and the tissues (Parodi 2015). The monitoring is usually performed by comparing the acquired data with the Monte Carlo simulated data of the patient treatment plan (Enghardt et al. 2004). The acquisition can be performed during irradiation at the treatment site (in-beam) or after beam delivery inside (in-room) or outside (off-line) the treatment room. Dedicated PET detectors integrated into the beam delivery systems are considered the elective choice for PET monitoring (Zhu and El Fakhri 2013) since the activity generated in tissue is at the highest level for both the long (^{11}C, ^{13}N, ^{15}O) and the short half time (^{10}C and ^{12}N) nuclides, the effect of the biological washout is minimized and patient repositioning errors are avoided.

In-beam PET monitoring has been clinically used between 1997 and 2008 on

more than 400 patients at the GSI Helmholtzzentrum für Schwerionenforschung in Darmstadt, Germany(Enghardt et al. 1999). The PET scanner installed at the GSI ion therapy facility was a double-head camera assembled from a commercial PET scanner integrated with the treatment unit. Recently another in-beam PET system has been installed at the proton gantry of the National Cancer Center Hospital in Kashiwa (Nishio et al. 2010), Japan, and used in clinic. The main problem to be addressed for an in-beam PET set-up is related to the irradiation induced background (mainly prompt photons and neutrons) (Testa et al. 2010, Biegun et al. 2012, Zhu and El Fakhri 2013). For syncrothron beams, the machine duty cycle is structured in a beam delivery phase (spill), in which the accelerated beam is extracted, and a pause (inter-spill), when the acceleration phase takes place. The typical cycle period is of few seconds. To avoid the influence of the background during the spill, the PET data acquisition is usually carried out during the inter-spill pauses only and for less than a minute post-irradiation (e.g., at GSI) (Enghardt et al. 1999). In this configuration, a considerable fraction of the induced activity is lost and the count statistics depends greatly on the accelerator duty cycle. For cyclotron-based facilities, the acquisition is complicated also by the continuous beam delivery and by the background induced by the passive beam shaping, so the PET signal is acquired after the end of the irradiation (e.g., in Kashiwa).

Therefore, in-beam systems operated in syncrotron facilities or in cyclotron facilities have not exploited so far the full potential of in-beam PET monitoring (Shakirin et al. 2011). However, substantial improvements in PET technology enabled the construction of higher performing in-beam systems. In (Sportelli et al. 2013) authors report beam-on operation of a dual head system at the CATANA protontherapy cyclotron facility in Catania, Italy, although the measurements were carried out at dose rates not directly comparable with clinical ones and for low energy beams. Beam-on measurements have also been carried out at synchrotron facilities as reported in (Shao et al. 2014, Kraan et al. 2015). However, in (Shao et al. 2014) data have been acquired during the whole irradiation period but only inter-spill data are used for evaluating the imaging performances of the system. In (Kraan et al. 2015) the experimental data, acquired both in-spill and inter-spill with the same system as in (Sportelli et al. 2013), have been summed up and then, off-line, subdivided in frames of different duration. The reconstructed profiles at increasing irradiation times have been compared with Monte Carlo simulations of the annihilation profiles. Data and simulation show a substantial disagreement for short irradiation periods (less than 30 sec), since the PET system was underperfoming due to the high count rate induced by the prompt radiation in the in-spill phase. These results suggest the importance of correctly acquire both the in-spill and inter-spill signals in order to filter the contribution of the background in the PET image and extract the valid signals from the induced positron emitters in the whole irradiation session. We refer to this acquisition modality as full-beam (Sportelli et al. 2013). To this aim, we have developed a PET detector system based on fast pixelated scintillators coupled one to one to silicon photomultlipliers. The read-out electronics system has been designed to cope with the count rate ex-

pected from syncrothron beams during the in-spill phase. Moreover, it provides the energy and the timestamp of each detected event for a time-resolved spectroscopic analysis of the acquired signals. The data acquisition system features a real-time monitoring of the electronics parameters and of selected physical properties, such as energy spectra and coincidence time resolution. The monitoring can be performed separately for in-spill and inter-spill data with the event selection based on the current single-event detection rate. The PET detector was tested at the Centro Nazionale di Adroterapia Oncologica (CNAO) in Pavia, Italy, the only dual ion (proton and carbon) therapy facility in Italy. Polymethyl methacrylate (PMMA) phantoms were irradiated with monoenergetic proton pencil beams of 68 MeV and 72 MeV and the secondary radiation emitted both in-spill and inter-spill has been acquired.

This paper is organised as follows. In the first part the PET detection system, the experimental set-up and and the data processing method are described. In particular, we present a filtering algorithm of the random events in the in-spill acquisitions based on the event selection at the synchrotron bunch level. In the second part we present the experimental results in terms of system performances and imaging capability for in-spill and inter-spill data sets, separately.

2 Materials and Methods

2.1 The PET detector

The PET detector used in this work is composed of two opposite detection modules of 5.12×5.12 cm^2 detection area, placed at 50 cm from each other. The module consists of an array of 16×16 pixelated ($3.2 \times 3.2 \times 20$ mm^3) Lutetium Fine Silicate (LFS) crystals coupled one to one to an array of 16×16 silicon photomultipliers, custom-made by the Hamamatsu Photonics company, Japan (Hamamatsu 2016).

Each module was read-out by four 64 channels TOFPET Front-End Application Specific Integrated Circuits (ASICs) (Rolo et al. 2013) hosted in a custom front-end board connected to a Xilinx ML605 FPGA mainboard. The system clock was 120 MHz. Two sensors were mounted on the front-end boards to monitor the temperature of the read-out system, which was kept constant at 36 °C by means of fans.

The PET scanner used in this work is a small prototype of the PET scanner that is being developed within the INSIDE project for the monitoring of particle therapy treatments of the head and neck (Fiorina et al. 2015, Marafini et al. 2015, Pennazio et al. 2015). The INSIDE PET scanner will be made of two planar panels, 10 cm wide and 25 cm long. Each panel will be composed of 10 detection modules used in this study. The LFS crystals coupled to silicon photomultipliers satisfy both requirements of compactness and speed of response. The 64 channels TOFPET ASIC has been chosen for the read-out of the detection modules because it provides the digitization of the time of interaction and

energy released with 100 kHz event rate per channel. Although the TOFPET ASIC is capable of performing Time Of Flight PET, the implementation of the time of flight was not a requirement of the INSIDE PET scanner, therefore the hardware design was not optimized to this purpose.

The control and acquisition software used in this study was adapted from the one developed within the INFN 4DMPET project (Morrocchi et al. 2013). The acquisition system is designed to cope with the rate of single events and save the data on a PC hard drive. Coincidence data analysis was performed off-line with a C++/BOOST based software. An on-line monitoring version of the coincidence analysis software based on the UDP protocol was also developed and successfully tested. The on-line monitor featured a Graphical User Interface (GUI) that allowed a real time visualization of relevant physical quantities and performance-assessment parameters.

2.2 Experimental set-up

Irradiation tests of PMMA phantoms were carried out at the CNAO ion therapy facility (Pavia, Italy). The PMMA phantoms ($4.9 \times 4.9 \times 7$ cm^3) were placed between the two PET modules with the long side parallel to the beam direction. The entrance surface of the phantoms was located 1 cm inside the PET Field Of View (FOV) while the exit surface was outside the FOV. The distance between the entrance surface of the detection module and the central axis of the PMMA phantoms was 25 cm. The layout (a) and the picture (b) of the experimental set-up are shown in figure 2.1. The beam direction and the spatial reference system used for the PET image reconstruction is also shown in 2.1 (a).

The CNAO synchrotron average beam time structure is of 1 s beam on (in-spill) followed by 4 s beam off (inter-spill). The beam intensity was varying in the $(1.1\text{-}2)\cdot10^9$ protons per spill (pps) range. The PMMA was irradiated with proton pencil beams impinging onto the center of the phantom entrance face. The energy of the beams was 68 and 72 MeV, corresponding to 36 and 40 mm Bragg peak depth in water, respectively. The total number of particle delivered for each session was $2\cdot10^{11}$. The PMMA phantom was changed after each acquisition, in order to avoid the residual activity from previous irradiations.

2.3 Data processing

2.3.1 Selection of the in-spill and inter-spill data

The data acquired with the PET detection system were saved in a single list mode that included both in-spill and inter-spill data.

The TOFPET ASIC provides the information of the trigger time (encoded as the event timestamp) and of the energy of each detected event. In a previous work (Piliero et al. 2015) it was shown that the rate of events detected as a function of the absolute time reproduces the pulsed structure of the beam. Such

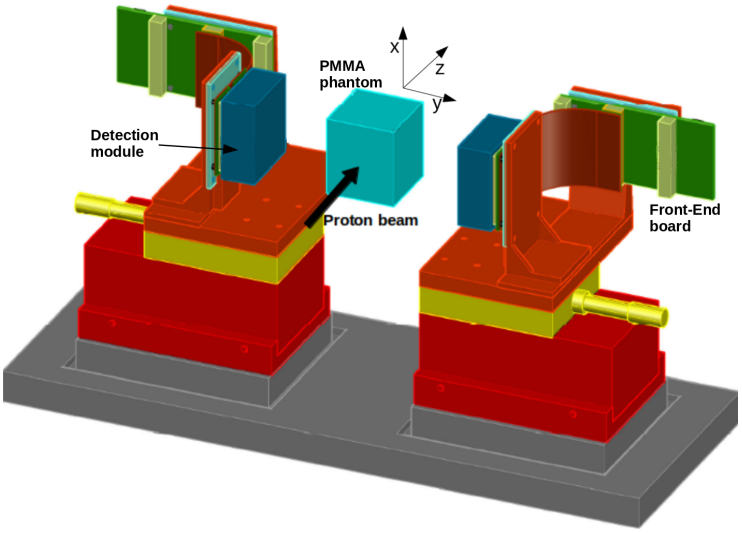

(a)

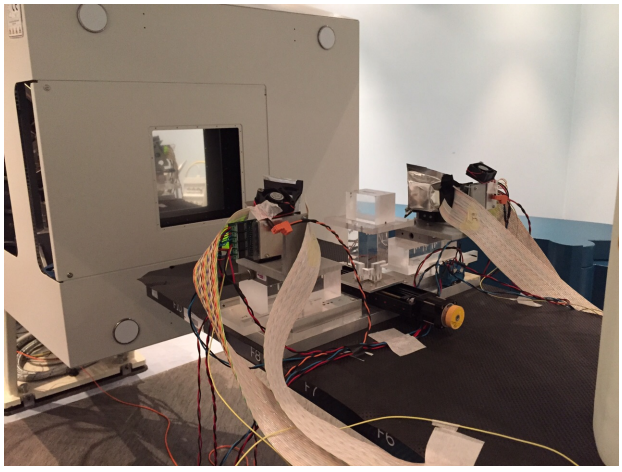

(b)

Figure 2.1: Layout of the experimental set-up, head-to-head distance is not to scale. The z-axis is parallel to the beam direction (a); the picture of the set-up at the CNAO treatment room. The beam nozzle is on the left (b).

feature was exploited to preprocess data and identify the spill intervals. The distribution of the single event rate as a function of time is shown in figure 2.2.

2.3.2 Selection of the coincidence data

PET images are based on the detection of coincidence events at the 511 keV annihilation peak. The TOFPET ASIC gives information on the energy of a detected event as a Time-Over-Threshold (ToT). The Time-Over-Threshold is a technique for processing charge pulses where information on the charge is given by the duration of the pulse. A threshold is set on both the rising edge and the falling edge of the pulse. A first time stamp is assigned when the pulse crosses the threshold on the rising edge and a second time stamp is assigned when the pulse crosses the threshold on the falling edge. The duration of the pulse is given by the difference between the two time stamps. A detailed description on how the Time-Over-Threshold technique is implemented in the TOFPET ASIC is given in reference (Rolo et al. 2013).

Before applying the coincidence search algorithm, the ToT range relative to the 511 keV annihilation peak was identified for each pixel of the detection modules. To do that, the ToT spectrum of a ^{68}Ge source placed between the two PET heads was acquired for each pixel and a gaussian fit was applied to the 511 keV photopeak. The fitting parameters (mean and σ) were saved and used to select the data acquired during the irradiation.

A coincidence search algorithm with an energy window of $\pm 2\sigma$ around the peak was applied to the experimental data. This energy window was chosen in order to select the photopeak events only and discard lower energy events in the tail of the Compton edge. The energy windows were therefore different for each pixel, depending on the sigma values of the gaussian fit. The variation of the sigma values among the pixels was about 15%.

The coincidence time window was set at 2 ns, consistent with a measured Coincidence Time Resolution of 400 ps (see subsection 3.2).

2.3.3 Image reconstruction

A Maximum Likelihood Estimation Maximization (MLEM) iterative image reconstruction algorithm was used to obtain the three-dimensional (3-D) spatial distribution of coincidence events (Vardi et al. 1985). Five iterations were used to reconstruct the images acquired in this work, with an execution time of about 1 s on a 3.40 GHz Intel Core i7-3770 CPU. This number of iterations is lower than the one usually performed in a full ring diagnostic scanner. The convergence rate of the MLEM algorithms depends on many factors including the scanner geometry, the system response matrix implementation and the number of data acquired by the scanner. In practical situations the MLEM algorithm is stopped before reaching the absolute convergence to achieve the desired level of signal to noise ratio. In this specific situation, where a small number of events was acquired compared to a full ring clinical scanner, we found that more than 15 iterations led to a rapid increase of the image noise. No substantial difference

in the images was found with a number of iterations between 5 and 15, therefore 5 iterations were considered the best compromise between image quality and computation speed.

The reconstructed FOV was $51.2\times51.2\times51.2$ mm^3 with 1.6 mm^3 voxels. Details about the reconstruction algorithm can be found in (Camarlinghi et al. 2014). The ImageJ software was used to visualize the reconstructed images.

2.3.4 β^+emitters activity profiles

Differences in beam energy or in the composition of the transversed material modify the spatial distribution of the generated β^+emitters. In case of a homogeneous phantom, a different proton beam energy leads to a different particle range and hence to a different length of the one-dimensional (1-D) profile of the PET image (herein called activity range). The 1-D activity profile was measured by plotting the values of the voxels in the central slice along the beam central axis, averaged over 4 voxels in the y direction (for axis references see figure 2.1 (a)). The distal fall-off of the profiles were fitted with the logistic function (Verhulst 1845) described by the following equation:

$$i = B + \frac{A - B}{1 + \mathrm{e}^{s(z-d)}} \tag{2.1}$$

where A and B are related to the maximum and minimum values of the image intensity i along the profile, s is the slope of the distal fall-off and d is the inflection point coordinate along the beam direction z. A and B depend on the actual beam intensity, treatment duration and data integration time, while d is closely related to the activity range inside the phantom. The difference between the d values at the two proton beam energies ($d(72MeV)$ - $d(68MeV)$) was evaluated for both the inter-spill and the in-spill data.

2.3.5 Processing of the in-spill events

During the spill, neutrons and photons are emitted promptly from the PMMA phantom as products of the interaction with the proton beam. High energy photons, like for example photons at 4 MeV or 6 MeV from the de-excitation of the ^{12}C and ^{16}O, are emitted immediately after the interaction of the proton with the nuclei, while neutrons are detected a few ns later (Biegun et al. 2012) because of their low velocity. As pointed out in (Crespo et al. 2005), the presence of prompt radiation increases the rate of random coincidences, therefore it might influence the 3-D spatial distribution of the coincidence events. In synchrotron based facilities, the radiation beam within the spill is characterized by bunches of tens of ns in width, equally spaced in time at the accelerator radiofrequency (RF). As a consequence, the prompt radiation is emitted only during the bunch period.

To study the influence of prompt radiation on the PET images it is necessary to assign each coincidence event to the time frame between two consecutive

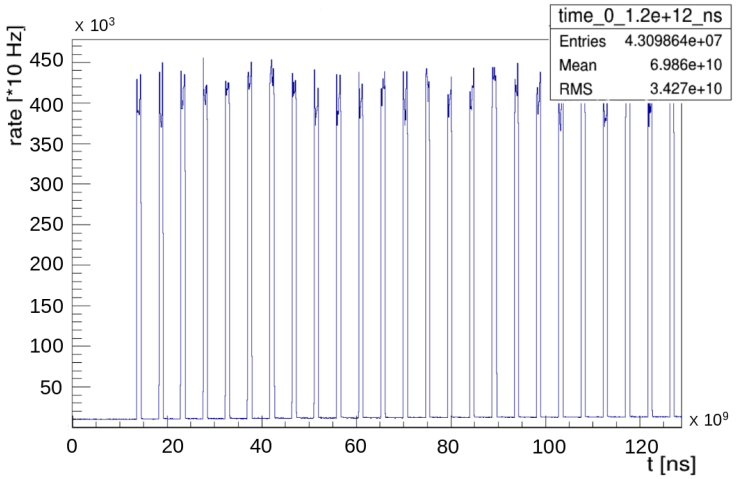

Figure 2.2: Distribution of single event rate as a function of time. The information on the rate was used to separate the in-spill from the inter-spill data.

bunches. This allows distinguishing for example the coincidence events acquired during the bunch from the ones acquired in the pause between two bunches. The experimental data were acquired in single list mode and each detected event carries the information of the energy and of the absolute time of detection since the start of the acquisition. To transform the absolute time values into time values within one acceleration period, the knowledge of the RF period, T_{RF} and of the absolute time of the first bunch is needed.

A plot of the rate of the single events detected within a spill did not show the temporal structure at the T_{RF} time scale because of low statistics, therefore the accelerator RF was measured by calculating the random coincidences with the delayed-coincidence method so as to increase the statistics over the whole acquisition time. A constant time delay value was added to the absolute time values of the events detected by one on the PET heads and the total number of random coincidences was calculated. The procedure was repeated for different time delay values ranging from 0 to 100 μs, with a 5 ns step. The resulting trend of random coincidences as a function of the time delay is characterised by peaks following the periodic microstructure of the beam at a sub-microsecond time scale, as also shown in reference (Parodi et al. 2005). The time separation between two peaks of the random distribution provides T_{RF} while the FWHM of the peaks provides an estimate of the bunch width after particle extraction, W_{ext}.

Since high energy prompt photons are emitted immediately after the interaction of the beam with the nuclei within the phantom, the time of the first bunch was chosen as the timestamp of the first detected event with an energy higher than 1 MeV (arbitrary threshold well above 511 keV) . Being the energy information stored as Time-Over-Threshold (ToT) value, the 1 MeV energy threshold

corresponds to a ToT of 300 ns. Time values Dt within one RF period were calculated as $Dt = t_{abs} - t_{bs}$, where t_{abs} is the absolute time of the event while t_{bs} is the bunch time. The time of the following bunch was chosen as the absolute timestamp of the first high energy event (ToT above 300 ns) with a Dt value greater than 590 ns. This time threshold takes into account the values of T_{RF} and W_{ext} previously calculated with the delayed-coincidence method. In literature Dt is usually measured with the Time of Flight (ToF) technique as in (Testa et al. 2010, Biegun et al. 2012).

3 Results and discussion

Single-spot irradiations of PMMA phantoms were performed with 68 MeV and 72 MeV proton beams. The data were acquired and saved in single list mode. The average single-event rate was 3.5 MHz in-spill and 150 kHz inter-spill. In-spill and inter-spill data were divided in two different groups and the 3-D activity distribution images were separately reconstructed.

3.1 Analysis of in-spill events

The total number of in-spill random coincidences as a function of the time delay value is shown in figure 3.1. The data show a modulation due to the ripple reduction technique that is used to deliver a uniform beam intensity during the spill [1]. The modulation frequency calculated by fitting the envelop of the peaks with a sinusoidal function is of 10 kHz. A sub-set of the data (black line) for a time delay interval of $3\mu s$ is shown in the inset of figure 3.1. The regular time pattern of the peaks related to the bunch time structure is clearly visible. The gaussian fit of the peaks (red line) provides an average W_{ext} of 138 ns.The average distance between two consecutive peaks provides a T_{RF} of 690 ns.

A plot of the ToT values as a function of Dt of each event is shown in figure 3.2. Dt=0 corresponds to the start of the bunch. Although the Dt values can be up to one RF period, the plot shown in figure 3.2 has been cut to 30 ns to highlight the time information regarding the prompt radiation and the neutrons. As expected, most of the high energy events, which are characterized by ToT values greater than 300 ns, are within the first ns (prompt gamma rays), and they are followed by lower energy events (bright spot in the range between 5 ns and 12 ns) that can be attributed to neutrons (Biegun et al. 2012) . The circled spot corresponds to 511 keV events likely due to annihilation of positrons produced via pair production by prompt photons (herein called prompt annihilations). Pair production occurs both in the PMMA and the crystal. The delay up to 2 ns can be attributed to the time of flight of the 511 keV photons travelling from the annihilation point to the detection point. For instance, one photon produced from positron annihilation in one LFS crystal can be detected in a crystal of the opposite head. In this case, considering the distance of 50 cm between the two PET heads, the time of flight is of 1.7 ns.

[1] private communication

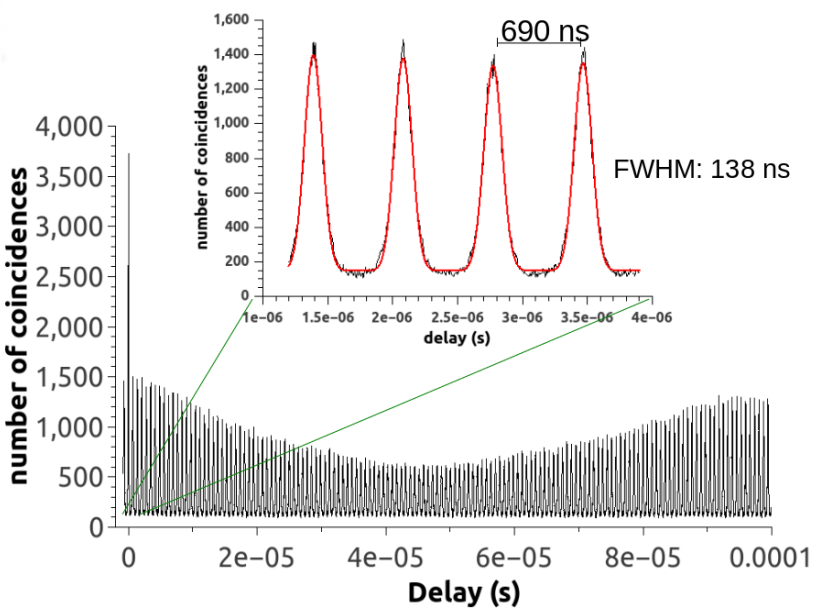

Figure 3.1: Total number of in-spill random coincidences versus the time delay applied to one head of the PET detector. The amplitude modulation is due to the ripple reduction technique applied at the CNAO beams. The inset shows peaks evenly spaced at the accelerator RF (black line) and their Gaussian fit (red line).

3.2 Coincidence Time Resolution

The Coincidence Time Resolution (CTR) distributions for the in-spill (dotted line) and inter-spill (solid line) data are shown in figure 3.3. The gaussian fit of the curves provides a FWHM of 1.16 ns inter-spill and of 1.30 ns in-spill. The in-spill distribution shows a higher background, which causes the Full Width at Tenth of Maximum (FWTM) to degrade from 1.96 ns inter-spill to 3.8 ns in-spill. This is likely due to the higher random coincidence rate, with a contribution of decreased ASIC performance at a rate different from the calibration one. The results of the CTR measurements, summarized in table 1, show no significant dependence on the beam energy. Improvements in CTR could be achieved by means of a fine ASIC calibration based on look-up tables, which was beyond the scope of this work. The distribution in figure 3.3 represented with a dashed line has been obtained by discarding the coincidence events with Dt values between 5 ns and 20 ns (comprising the bright spot in figure 3.2). Since these events

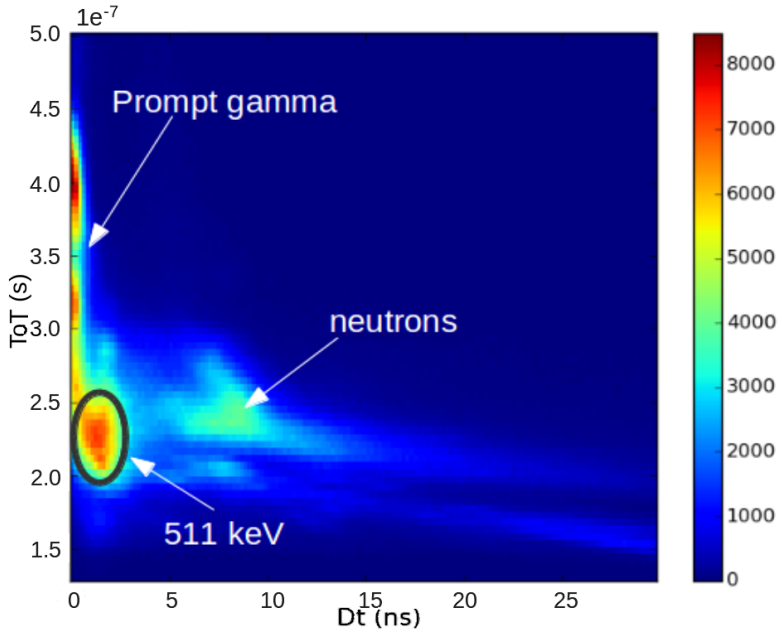

Figure 3.2: Plot of the events ToT as a function of Dt. Higher ToT values refer to high energy events. The circled spot corresponds to 511 keV events likely due to annihilation of positrons produced via pair production by prompt photons (herein called prompt annihilations). The bright spot in the range between 5 ns and 12 ns is attributed in the literature to neutrons background (Biegun et al. 2012).

have been attributed to neutrons, we refer to this noise suppression algorithm as neutron filter. Although most of the neutrons have Dt values between 5 ns and 15 ns, coincidence events with Dt values up to 20 ns were included in the neutron filter algorithm to decrease as much as possible the number of random coincidences due to the neutrons background. As shown in figure 3.3, the background contribution, once applied the neutron filter (dashed line), decreases by a factor two with respect to the one without filter (dotted line), while the total number of accepted in-spill coincidences decreases by 12%.

3.3 1-D activity profiles

Figure 3.4 shows the 1-D activity profiles for the inter-spill data at 68 MeV (black dots) and 72 MeV (red dots). The profiles were fitted (respectively black and red dotted lines) with the sigmoid function described in equation 2.1 to evaluate the activity range difference. Both data sets (in-spill and inter-spill) show an activity range difference in sub-millimeter agreement with the proton range difference in PMMA for 68 and 72 MeV calculated from the NIST database, that is of 3.64 mm (Berger et al. 2005). A summary of the expected and measured values is listed in table 2. The uncertainties are calculated propagating errors resulting from data fit.

The detector imaging performance was also evaluated for the dose delivered in a typical treatment session (i.e., about 2 Gy). The data was filtered to accept only the data acquired during the first 10 spills, which roughly correspond to 2 Gy in water. The image quality decreases because of both reduced acquisition time and lower phantom activation. The sigmoid fit parameters show a higher uncertainty. Still, the measured range difference is 3.04 $\pm$ 0.76 mm.

Beam Energy	*Measure*	*FWHM(ns)*	*FWTM(ns)*
68 MeV	Inter-spill	1.26	2.06
	In-spill	1.4	3.4
72 MeV	Inter-spill	1.16	1.94
	In-spill	1.3	3.8

Table 1: Coincidence Time Resolution FWHM and FWTM for the inter-spill and in-spill acquisitions at respectively 68 and 72 MeV.

Measure	*Range difference (mm)*	*uncertainty (mm)*
Theoretical value (Berger et al. 2005)	3.64	-
All inter-spill data	3.61	0.10
First 10 inter-spill	3.04	0.76
In-spill	3.80	0.31

Table 2: Expected and measured range differences for protons at 72 and 68 MeV. The uncertainties are calculated propagating errors resulting from data fit.

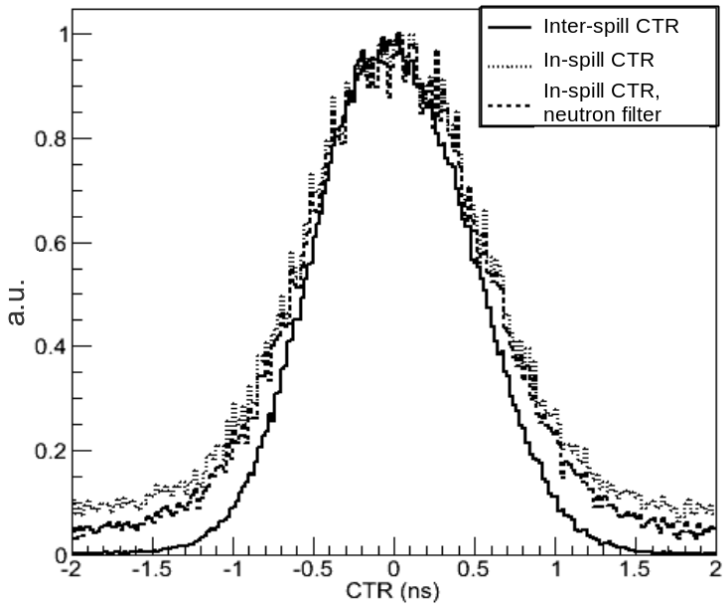

Figure 3.3: Coincidence Time Resolution distributions for inter-spill (solid line), in-spill (dotted line) and in-spill neutron-filtered (dashed line) datasets, for a 72 MeV proton beam impinging on a PMMA phantom.

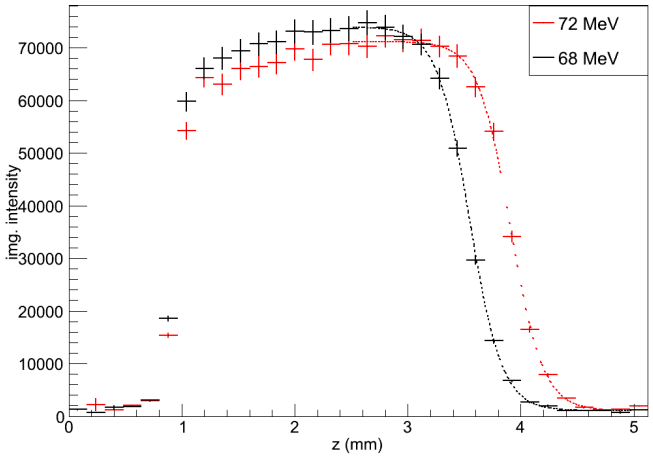

Figure 3.4: 1-D activity profiles at 68 (black) and 72 MeV (red) with sigmoid fit. The image intensity is the voxel value, which is proportional to the activity contained in each voxel.

3.4 Coincidence events spatial distributions

Figure 3.5 shows the central slice of the 3-D coincidence events spatial distribution (y-z projection) relative to the inter-spill data (a) and the in-spill data (b) related to the 72 MeV acquisition. The beam enters from the left side. The in-spill distribution is noisier than the inter-spill one due to the limited statistics (the in-spill fraction is only 20% of the whole acquisition time) and to the prompt radiation background. In particular coincidence events are present before the entrance surface of the phantom (outside the activated area) and a long tail is observed in the distal part of the reconstructed activity. To study the influence of prompt radiation, the in-spill data were filtered to select true coincidence events occurring during the pauses between two consecutive bunches.

Discarding the events with Dt values between 0 and 20 ns (events attributed to prompt radiation and neutrons as shown in figure 3.2), more than 87% of the coincidence events in the in-spill dataset were cut out. This suggests that the in-spill PET images are mostly formed by the prompt annihilation events (circled spot in figure 3.2). Moreover, the lack of coincidences after the first tens of ns can be explained by saturation effects of the data acquisition system so that some events might have not been collected. Further tests with reduced beam currents and with radioactive sources are required to investigate this behaviour. In addition the implementation of fast trigger and veto schemes for the acquisition of the events in the pauses between the bunches is underway.

Still, after applying the neutron filter, the counts at the entrance of the phantom decreases significantly as shown in figure 3.6 (a). Therefore the activity

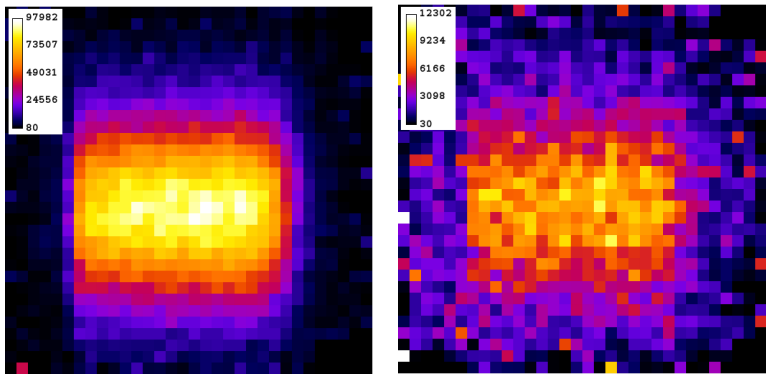

(a) (b)

Figure 3.5: Central slice in the y-z plane of the 3-D coincidence events spatial distribution related to the 72 MeV acquisition: inter-spill data (a) and in-spill data (b). Numbers in the colormap refer to the image intensity values which are proportional to the activity contained in each voxel.

before the phantom was likely due to beam induced neutron background.

The tail at the end of the activity range is not influenced by the neutron filter. It probably could be due to the large positron range of short-lived β^+ emitters, such as ^{12}N (Dendooven et al. 2015), and to the prompt annihilations (Kraan et al. 2015). The 1-D activity profiles for inter-spill (black), in-spill (red) and in-spill neutron filtered are shown (green) in figure 3.6 (b).

A 2 mm longer activity range was measured with the in-spill data compared to the inter-spill data. Artifacts in the image due to the geometrical acceptance of the detection system were excluded. In a previous work (Fiorina et al. 2015) Monte Carlo simulations of the experimental set up described in this study were carried out. The simulations were divided in two steps: in the first one the beam interactions with the phantom were simulated. The output of this step was the activity distribution induced in the phantom. In the second step, the detector performance and the reconstruction process are taken into account. The output of the second step was the 3D PET image. The comparison between the simulated activity distribution (output of the first step of the simulation) and the experimental image did not show any appreciable difference. This result excludes the introduction of artifacts in the reconstruction process. The difference in the in-spill and inter-spill profile ranges is still under investigation, even though an explanation could be found in the different nuclear reactions leading to the production of prompt gamma rays and positron emitters. Due to lower reaction thresholds (few MeV) (Kozlovsky et al. 2002), the prompt photons spatial distribution extends closer to the distal edge of the Bragg peak than the positron emitter distribution (reaction threshold higher than 10 MeV).

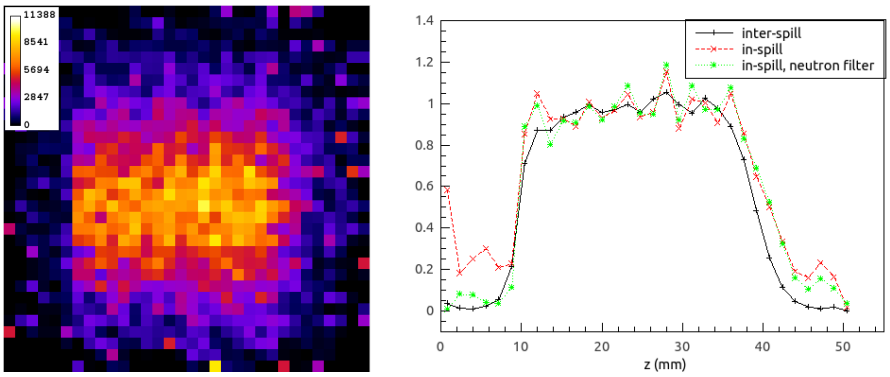

(a) (b)

Figure 3.6: Central slice in the y-z plane of the 3-D coincidence events distribution after applying the neutron filter (a); 1-D activity profiles for inter-spill (black), in-spill (red) and in-spill neutron-filtered (green) coincidence events (b). Numbers in the colormap refer to the image intensity values which are proportional to the activity contained in each voxel.

4 Conclusions

A PET detector prototype was tested at the CNAO ion therapy facility by irradiating PMMA phantoms with monoenergetic proton beams of 68 MeV and 72 MeV.

Data were acquired in single list mode and then filtered to separate the in-spill and the inter-spill data sets, in oder to separately assess the PET detector performances. The average measured single-event rate was 3.5 MHz in-spill and 150 kHz inter-spill. Experimental measurements included the evaluation of the coincidence time resolution (CTR) and of the β^+ emitting radioisotopes activity range.

The in-spill and inter-spill CTR showed similar behaviour (1.3 and 1.16 ns FWHM respectively), although the first presented a higher random background rate due to the secondary particles emitted during and immediately after the beam bunches. No significant energy dependence was observed.

A MLEM iterative image reconstruction algorithm was used to obtain the 3-D spatial distribution of the coincidence events. Two separate images were reconstructed with the in-spill and the inter-spill data. The 1-D activity profiles were measured by projecting the images along the beam direction. The evaluation of the absolute value of the proton range from the measurement of the activity distributions is not straightforward. However the difference in the proton ranges at the two energies could be estimated from the difference in the activity ranges. Activity ranges were evaluated for the 68 MeV and 72 MeV data sets. The difference between the two activity ranges was in sub-millimeter

agreement with the expected proton range difference, using either the in-spill or the inter-spill data, including the case of the 2 Gy (typical dose delivered in a fraction) data subset.

Starting from the analysis of the in-spill events, we developed a selection algorithm based on the energy and the time of flight of the events between two consecutive bunches (herein called neutron filter). This filter allowed the reduction of a factor two of the random background in the in-spill coincidence time distribution.

The neutron filter was also effective in discriminating the random contribution due to neutron reactions and then in reducing the image background at the phantom entrance in the in-spill images. The implementation of fast trigger and veto techniques to acquire experimental data only in the pauses between the bunches is underway.

A 2 mm longer activity range was measured with the in-spill data compared to the inter-spill data. This effect, likely due to the prompt photons contribution in the in-spill images, needs further investigation and might require the implementation of a calibration stage and the evaluation of a correction factor to be applied to data taken during the beam delivery. Still, the difference in the in-spill activity range at two different beam energies is in agreement with the difference measured with the inter-spill data.

The detector used for this analysis is a small prototype of the in-beam PET system being developed within the INSIDE project (Marafini et al. 2015, Pennazio et al. 2015, Fiorina et al. 2015). INSIDE is a bi-modal system that combines an in-beam PET scanner and a particle tracking system, as a single imaging device. It is designed to detect at the same time annihilation photons and charged secondary particles. The PET scanner, tailored for the imaging of head and neck tumours, is made of two planar detectors of (10 x 25) cm^2. The PET activity map created in the target will be complemented by the beam profile, obtained by tracking the secondary particles (protons) coming from the interaction of the primary beam with the target nuclei and from projectile fragmentation for carbon beams. The full in-beam PET system has been recently installed at CNAO and it is at present in commissioning phase.

Future works will focus on tests with proton and ion beams, including actual tumour treatment plans, in order to assess the PET scanner monitoring capability in a clinical environment. The geometrical acceptance of the INSIDE PET scanner is ten times higher than the prototype used in this work, therefore the same precision in the range measurement is expected within even shorter acquisition time.

The results of this work are a good indication that such a PET system can successfully operate in-beam at synchrotron-based facilities without modifying the clinical workflow. In-spill acquisition feasibility was investigated. At present, the CNAO synchrotron duty cycle, characterized by 1 s of spill time and 4 seconds of inter-spill, allows the acquisition of a satisfactory amount of PET data during the inter-spill only. However, an improvement of the duty cycle aiming at shorter treatments at the same dose is foreseen. In this scenario the inter-spill interval will be reduced as much as possible and the contribution of

the in-spill data to the statistics will be then determinant. This consideration is even more true in case of cyclotrons where the in-spill data is the only source of data.

Acknowlegements

This work has been mainly supported by the Italian Ministry of University and Research (MIUR) under the program PRIN 2010-2011 - INSIDE project 2010P98A75. The authors are also very grateful to CNAO personnel, particularly to Mario Ciocca, Marco Donetti, Marco Pullia and S. Rossi and to Simona Giordanengo (INFN-Torino) for their kind collaboration in the data acquisition and the discussion of results.

References

Berger M J, Coursey J S, Zucker M A and Chang J 2005 ESTAR, PSTAR, and ASTAR: Computer Programs for Calculating Stopping-Power and Range Tables for Electrons, Protons, and Helium Ions (version 1.2.3).
URL: *http://physics.nist.gov/PhysRefData/Star/Text/PSTAR.html*

Biegun A K, Seravalli E, Lopes P C, Rinaldi I, Pinto M, Oxley D C, Dendooven P, Verhaegen F, Parodi K, Crespo P and Schaart D R 2012 Time-of-flight neutron rejection to improve prompt gamma imaging for proton range verification: a simulation study *Physics in Medicine and Biology* **57**(20), 6429.

Camarlinghi N, Sportelli G, Battistoni G, Belcari N, Cecchetti M, Cirrone G A P, Cuttone G, Ferretti S, Kraan A, Retico A et al. 2014 An in-beam PET system for monitoring ion-beam therapy: test on phantoms using clinical 62 MeV protons *Journal of Instrumentation* **9**(04), C04005.

Crespo P, Barthel T, Frais-Kolbl H, Griesmayer E, Heidel K, Parodi K, Pawelke J and Enghardt W 2005 Suppression of Random Coincidences During In-Beam PET Measurements at Ion Beam Radiotherapy Facilities *IEEE Transactions on Nuclear Science* **52**(4), 980–987.

Del Guerra A, Belcari N and Bisogni M G 2016 Positron Emission Tomography: Its 65 years *La Rivista del Nuovo Cimento* **39**(4), 155–223.

Dendooven P, Buitenhuis H J T, Diblen F, Heeres P N, Biegun A K, Fiedler F, Goethem M J v, Graaf E R v d and Brandenburg S 2015 Short-lived positron emitters in beam-on PET imaging during proton therapy *Physics in Medicine and Biology* **60**(23), 8923.

Enghardt W, Debus J, Haberer T, Hasch B G, Hinz R, Jäkel O, Krämer M, Lauckner K, Pawelke J and Pönisch F 1999 Positron emission tomography for

quality assurance of cancer therapy with light ion beams *Nuclear Physics A* **654**(1, Supplement 1), 1047c–1050c.

Enghardt W, Parodi K, Crespo P, Fiedler F, Pawelke J and Pönisch F 2004 Dose quantification from in-beam positron emission tomography *Radiotherapy and Oncology* **73, Supplement 2**, S96 – S98. Carbon-Ion TheraphyProceedings of the Heavy Charged Particles in Biology and Medecine.

Fiorina E et al. 2015 An integrated system for the online monitoring of particle therapy treatment accuracy *Nuclear Instruments and Methods in Physics Research Section A: Accelerators, Spectrometers, Detectors and Associated Equipment* .

Golnik C, Hueso-González F, Müller A, Dendooven P, Enghardt W, Fiedler F, Kormoll T, Roemer K, Petzoldt J, Wagner A et al. 2014 Range assessment in particle therapy based on prompt γ-ray timing measurements *Physics in medicine and biology* **59**(18), 5399.

Hamamatsu 2016.
URL: *http://www.hamamatsu.com/*

Kim D, Yim H and Kim J 2009 Pinhole camera measurements of prompt gamma-rays for detection of beam range variation in proton therapy *Journal of the Korean Physical Society* **55**(4), 1673–1676.

Kormoll T, Fiedler F, Schöne S, Wüstemann J, Zuber K and Enghardt W 2011 A Compton imager for in-vivo dosimetry of proton beams-a design study *Nuclear Instruments and Methods in Physics Research Section A: Accelerators, Spectrometers, Detectors and Associated Equipment* **626**, 114–119.

Kozlovsky B, Murphy R J and Ramaty R 2002 Nuclear deexcitation gamma-ray lines from accelerated particle interactions *The Astrophysical Journal Supplement Series* **141**(2), 523.

Kraan A C, Battistoni G, Belcari N, Camarlinghi N, Ciocca M, Ferrari A, Ferretti S, Mairani A, Molinelli S, Pullia M et al. 2015 Online monitoring for proton therapy: A real-time procedure using a planar PET system *Nuclear Instruments and Methods in Physics Research Section A: Accelerators, Spectrometers, Detectors and Associated Equipment* **786**, 120–126.

Lee H R, Park J H, Kim H S, Kim C H and Kim S 2013 Two-dimensional measurement of the prompt-gamma distribution for proton dose distribution monitoring *Journal of the Korean Physical Society* **63**(7), 1385–1389.

Llosá G, Cabello J, Callier S, Gillam J E, Lacasta C, Rafecas M, Raux L, Solaz C, Stankova V, de La Taille C et al. 2013 First compton telescope prototype based on continuous LaBr 3-SiPM detectors *Nuclear Instruments and Methods in Physics Research Section A: Accelerators, Spectrometers, Detectors and Associated Equipment* **718**, 130–133.

Marafini M, Frallicciardi P M, Faccini R, Morone C, Voena C, Patera V, Piersanti L, Sciubba A, Attili A et al. 2015 The INSIDE Project: Innovative Solutions for In-Beam Dosimetry in Hadrontherapy. *Acta Physica Polonica, A.* **127**(5).

McCleskey M, Kaye W, Mackin D, Beddar S, He Z and Polf J 2015 Evaluation of a multistage CdZnTe Compton camera for prompt γ imaging for proton therapy *Nuclear Instruments and Methods in Physics Research Section A: Accelerators, Spectrometers, Detectors and Associated Equipment* **785**, 163–169.

Morrocchi M, Ambrosi G, Bisogni M G, Cerello P, Corsi F, Ionica M, Marino N, Marzocca C, Pennazio F, Pirrone G, Santoni C, Wheadon R and Del Guerra A 2013 Development of a PET detector module with Depth of Interaction capability *Nuclear Instruments and Methods in Physics Research Section A: Accelerators, Spectrometers, Detectors and Associated Equipment* **732**, 603–606.

Nishio T, Miyatake A, Ogino T, Nakagawa K, Saijo N and Esumi H 2010 The development and clinical use of a beam ON-LINE PET system mounted on a rotating gantry port in proton therapy *International Journal of Radiation Oncology* Biology* Physics* **76**(1), 277–286.

Parodi K 2015 Vision 20/20: Positron emission tomography in radiation therapy planning, delivery, and monitoring *Medical Physics* **42**(12), 7153–7168.

Parodi K 2016 On- and off-line monitoring of ion beam treatment *Nuclear Instruments and Methods in Physics Research Section A: Accelerators, Spectrometers, Detectors and Associated Equipment* **809**, 113–119.

Parodi K, Crespo P, Eickhoff H, Haberer T, Pawelke J, Schardt D and Enghardt W 2005 Random coincidences during in-beam PET measurements at microbunched therapeutic ion beams *Nuclear Instruments and Methods in Physics Research Section A: Accelerators, Spectrometers, Detectors and Associated Equipment* **545**(1), 446–458.

Pennazio F, Attili A, Cerello P, Coli S, Giraudo G, Rivetti A, Wheadon R, Fiorina E, Peroni C, Battistoni G et al. 2015 A study of Monitoring Performances with the INSIDE System. *Acta Physica Polonica, A.* **127**(5).

Perali I, Celani A, Bombelli L, Fiorini C, Camera F, Clementel E, Henrotin S, Janssens G, Prieels D, Roellinghoff F, Smeets J, Stichelbaut F and Vander F S 2014 Prompt gamma imaging of proton pencil beams at clinical dose rate *Physics in Medicine and Biology* **59**(19), 5849.

Piliero M A, Bisogni M G, Cerello P, Del Guerra A, Fiorina E, Liu B, Morrocchi M, Pennazio F, Pirrone G and Wheadon R 2015 Performance of a fast acquisition system for in-beam PET monitoring tested with clinical proton beams *Nuclear Instruments and Methods in Physics Research Section A: Accelerators, Spectrometers, Detectors and Associated Equipment* **804**, 163–166.

Richter C, Pausch G, Barczyk S, Priegnitz M, Keitz I, Thiele J, Smeets J, Stappen F V, Bombelli L, Fiorini C, Hotoiu L, Perali I, Prieels D, Enghardt W and Baumann M 2016 First clinical application of a prompt gamma based in vivo proton range verification system *Radiotherapy and Oncology* .

Roellinghoff F, Richard M H, Chevallier M, Constanzo J, Dauvergne D, Freud N, Henriquet P, Le Foulher F, Létang J, Montarou G et al. 2011 Design of a compton camera for 3D prompt-γ imaging during ion beam therapy *Nuclear Instruments and Methods in Physics Research Section A: Accelerators, Spectrometers, Detectors and Associated Equipment* **648**, S20–S23.

Rolo M D, Bugalho R, Gonçalves F, Mazza G, Rivetti A, Silva J C, Silva R and Varela J 2013 TOFPET ASIC for PET applications *Journal of Instrumentation* **8**(02), C02050.

Shakirin G, Braess H, Fiedler F, Kunath D, Laube K, Parodi K, Marlen Priegnitz and Enghardt W 2011 Implementation and workflow for PET monitoring of therapeutic ion irradiation: a comparison of in-beam, in-room, and off-line techniques *Physics in Medicine and Biology* **56**(5), 1281.

Shao Y, Sun X, Lou K, Zhu X R, Mirkovic D, Poenisch F and Grosshans D 2014 In-beam PET imaging for on-line adaptive proton therapy: an initial phantom study *Physics in Medicine and Biology* **59**(13), 3373.

Sportelli G, Belcari N, Camarlinghi N, Cirrone G A P, Cuttone G, Ferretti S, Kraan A, Ortuno J E, Romano F, Santos A, Straub K, Tramontana A, Guerra A D and Rosso V 2013 First full-beam PET acquisitions in proton therapy with a modular dual-head dedicated system *Physics in Medicine and Biology* **59**(1), 43.

Testa M, Bajard M, Chevallier M, Dauvergne D, Freud N, Henriquet P, Karkar S, Foulher F L, Létang J M, Plescak R, Ray C, Richard M H, Schardt D and Testa E 2010 Real-time monitoring of the Bragg-peak position in ion therapy by means of single photon detection *Radiation and Environmental Biophysics* **49**(3), 337–343.

Vardi Y, Shepp L A and Kaufman L 1985 A Statistical Model for Positron Emission Tomography *Journal of the American Statistical Association* **80**(389), 8–20.

Verburg J M and Seco J 2014 Proton range verification through prompt gamma-ray spectroscopy *Physics in medicine and biology* **59**(23), 7089.

Verhulst P F 1845 Recherches mathématiques sur la loi d'accroissement de la population. *Nouveaux Mémoires de l'Académie Royale des Sciences et Belles-Lettres de Bruxelles* **18**, 14–54.

Zhu X and El Fakhri G 2013 Proton therapy verification with PET imaging *Theranostics* **3**(10), 731.